Physics-Informed Bayesian MCMC Analysis of Krypton/Argon Sputter Yields[*†]

Henry Huh[‡]
Exquadrum, Air Force Research Laboratory
Edwards Air Force Base, CA, 93524, USA

David L. Bilyeu[§]
Air Force Research Laboratory, Edwards Air Force Base, CA, 93524, USA

John T. Yim[¶]
NASA Glenn Research Center, Cleveland, OH, 44135, USA

1 Abstract

Electric propulsion spacecraft increasingly require alternative propellants like krypton and argon due to xenon's high cost, yet critical sputter yield data for these propellants remain severely limited across diverse spacecraft materials. Traditional empirical fitting approaches are limited by high-dimensional parameter estimation with sparse data, resulting in poorly constrained predictions essential for spacecraft integration. We develop a physics-informed Bayesian Markov Chain Monte Carlo framework that addresses this data scarcity by transferring knowledge from well-characterized xenon systems to data-limited Kr and Ar combinations through Lindhard-Scharff-Schiøtt (LSS) collision theory. Our approach employs LSS scaling predictions as Gaussian prior distributions, effectively constraining the parameter search space and addressing the dimensionality problem encountered in previous methods. Testing on metallic and covalent material systems, our physics-informed methodology achieves five to twenty-fold reductions in parameter uncertainty compared to independent empirical fitting, enabling reliable cross-species predictions for spacecraft design applications.

[‡]Research Scientist, In-Space Propulsion Branch, henry.huh.1.ctr@us.af.mil

[§]Modeling and Simulation Group Lead, In-Space Propulsion Branch, david.bilyeu.1@spaceforce.mil

[¶]Aerospace Technologist, Electric Propulsion systems branch, john.t.yim@nasa.gov

2 Nomenclature

Y	Sputter yield [atoms/ion]	Q	Scaling factor [atoms/ion]
E	Ion energy [eV]	λ	Onset parameter
E_{th}	Threshold energy [eV]	μ	Transition sharpness exponent
s_n	Reduced nuclear stopping power	S_n	Nuclear stopping cross section [eV·m^2]
M_i	Ion mass [amu]	M_s	Target atom mass [amu]
Z_i	Ion atomic number	Z_s	Target atomic number
ε	Reduced energy	a_L	Lindhard screening length [m]
U_s	Surface binding energy [eV]	e	Elementary charge [C]
α_S	Energy transfer factor	π	Pi constant
m_r	Reduced mass $\frac{M_i M_s}{M_i+M_s}$	N	Atomic density [atoms/m^3]
n	Power-law exponent	$\boldsymbol{\theta}$	Parameter vector
$\mathcal{L}$	Likelihood function	Y_{model}	Model prediction [atoms/ion]
Γ_a	Flux of ejected atoms [atoms/s]	Γ_i	Flux of incident ions [ions/s]
s_n^{KC}	KC potential nuclear stopping	a_0	Bohr radius [m]
$T_{\max}$	Maximum energy transfer [eV]	s	Yamamura model exponent
α	Empirical exponent for $Z_i Z_s$ scaling	β	Empirical exponent for mass scaling
$\Phi(\varepsilon)$	Universal nuclear stopping function	i	Index variable
E_i	Experimental energy data [eV]	Y_i	Experimental yield data [atoms/ion]
σ_i	Experimental uncertainty	θ	Incident angle [°]
tar	Target system	ref	Reference system

3 Introduction

Xenon has been widely adopted for electric propulsion missions due to its favorable properties, including low ionization energy and high momentum transfer efficiency. However, the high cost of xenon makes alternative propellants such as krypton and argon attractive candidates for missions where performance requirements can be met with these lower-cost options. While extensive sputter yield databases exist for xenon, comparable data for krypton and argon systems remain limited, resulting in significant uncertainties when modeling plume-surface interactions for these alternative propellants.

Sputter yield prediction involves fitting complex semi-empirical models to experimental data that are often sparse and uncertain. The field of sputter yield modeling has evolved through several distinct eras, beginning with early collision cascade theory developed by Sigmund in the 1960s-70s [1]. This foundation was extended through empirical refinements in the 1990s-2000s, most notably through energy-dependent empirical formulas and comprehensive databases of fitting parameters developed by Yamamura and others [2–5]. The field subsequently transitioned into computational approaches dominated by Monte Carlo simulations. The Transport of Ions in Matter (TRIM) code, developed by Biersack and Haggmark in 1980, was expanded into the comprehensive Stopping and Range of Ions in Matter (SRIM) software package by Ziegler and Biersack around 1983, becoming the industry standard for ion-solid interaction modeling [6, 7]. However, experimental studies by Nakles revealed significant limitations of these simulation approaches at low energies relevant to electric propulsion applications [8]. More recently, reduced-order analytical models have been developed by Biswas et al. for facil-

ity sputtering analysis as part of comprehensive collaborative programs such as the Joint Advanced Propulsion Institute (JANUS) project [9], while advanced molecular dynamics simulations have been developed by Tran for specific ion-target combinations such as Xe-C systems, though these remain computationally expensive for broader applications [10]. Currently, the field is characterized by a practical divide: industry applications rely heavily on SRIM simulations with selective experimental validation, while academic research emphasizes advanced statistical methods combined with empirical models such as those developed by Eckstein [11].

Bayesian Markov-Chain Monte Carlo (MCMC) methods provide a robust framework for this challenge by treating model parameters as probability distributions, enabling proper uncertainty quantification and avoiding overfitting common in traditional least-squares approaches. Yim successfully applied Bayesian MCMC to xenon sputtering data, providing a framework for uncertainty quantification [12]. However, high-dimensional parameter fitting with limited data remains a fundamental challenge in sputter yield modeling, leading to under-constrained parameter estimates and large uncertainties. This problem becomes especially challenging for krypton and argon systems, where the scarcity of experimental data makes independent parameter fitting unreliable, leading to weakly constrained predictions. To address these limitations, we develop a physics-informed framework that leverages Lindhard-Scharff-Schiøtt (LSS) collision theory to transfer knowledge from well-characterized reference systems to data-limited Kr and Ar combinations [13].

Our approach uses LSS scaling predictions as Gaussian prior distributions in the Bayesian framework, effectively constraining the parameter search space and addressing the dimensionality problem encountered in previous approaches. This enables accurate cross-species and cross-material (different target materials) predictions with reliable uncertainty bounds essential for spacecraft integration applications.

4 Background and Approach

4.1 Energy-Dependent Sputter Yield Models

When an ion strikes a target surface with an energy greater than a threshold binding energy, one or more target atoms or molecules can be ejected. The process is described by the binary collision approximation, where momentum transfer cascades through collisions inside the material. The sputtering yield is defined as

$$Y = \frac{\Gamma_a}{\Gamma_i} = \frac{\text{Atoms ejected}}{\text{Ions incident}} \tag{1}$$

where Γ_a and Γ_i are the fluxes of ejected atoms and incident ions, respectively. For $E > E_{th}$, Y often follows a power-law:

$$Y \propto (E - E_{th})^n \tag{2}$$

The Sigmund model [1] gives

$$Y = \frac{3\alpha_S}{4\pi^2} \frac{S_n(E)}{NU_s} \tag{3}$$

Here, $S_n(E)$ is the dimensional nuclear stopping power (energy loss per path length), while $s_n(\varepsilon)$ used later is its dimensionless form, depending only on reduced energy ε.

$\alpha_S = \frac{4M_iM_s}{(M_i+M_s)^2}$ is the energy transfer factor, N the atomic density, and U_s the surface binding energy. While insightful, Eq. (3) underpredicts low-energy yields relevant to EP.

Eckstein's formulation [14] captures threshold behavior more flexibly:

$$Y = Q \cdot s_n \cdot \frac{\left(\frac{E}{E_{th}} - 1\right)^{\mu}}{\lambda + \left(\frac{E}{E_{th}} - 1\right)^{\mu}} \tag{4}$$

where Q is a scaling factor [atoms/ion], λ the onset parameter, μ the sharpness exponent, and E_{th} the threshold energy [eV]. Other notable forms include Yamamura [15] and Bohdansky [16]:

$$Y = Q \cdot s_n \cdot \left[1 - \sqrt{\frac{E_{th}}{E}}\right]^{s} \tag{5}$$

$$Y = Q \cdot s_n \cdot \left[1 - \left(\frac{E_{th}}{E}\right)^{2/3}\right] \cdot \left[1 - \frac{E_{th}}{E}\right]^{2} \tag{6}$$

All use the nuclear stopping cross-section s_n, often expressed via the KC potential [17]:

$$s_n^{KC} = \frac{0.5 \ln(1 + 1.2288\varepsilon)}{\varepsilon + 0.1728\sqrt{\varepsilon} + 0.008\varepsilon^{0.1504}} \tag{7}$$

with reduced energy

$$\varepsilon = \frac{a_L E}{Z_i Z_s e^2} \cdot \frac{M_s}{M_i + M_s}, \quad a_L = \frac{0.8854 a_0}{Z_i^{0.23} + Z_s^{0.23}}, \tag{8}$$

where a_L is the Lindhard screening length from Thomas–Fermi theory.

4.2 LSS Cross-Species/Materials Scaling Theory

Building upon these energy-dependent models and addressing the data scarcity challenges outlined in the introduction, we implement a three-stage methodology: (1) comprehensive fitting of well-characterized reference systems, (2) physics-informed parameter scaling via universal LSS collision theory, and (3) Bayesian refinement using target system data. Rather than fitting each ion-target combination independently with broad empirical priors, we leverage Lindhard-Scharff-Schiøtt (LSS) collision theory [18] to establish physics-informed prior distributions that enable systematic parameter transfer across both ion species and target materials.

While LSS theory enables parameter transfer between any ion-target combinations, we select xenon systems as references due to their extensive experimental databases and direct relevance to electric propulsion applications. Using material-appropriate xenon reference systems (molybdenum for metallic targets with 110 experimental points, carbon for covalent materials with 44 experimental points), the Eckstein model parameters scale to Kr/Ar systems across different target materials according to fundamental collision physics:

From LSS, Q in Eq. (4) scales with the ratio of nuclear stopping power to U_s:

$$Q \propto \frac{S_n(E)}{U_s} \propto Z_i Z_s \cdot m_r \tag{9}$$

where $m_r = \frac{M_i M_s}{M_i + M_s}$ is the reduced mass. Since E-dependence is already in s_n, Eq. (9) reflects only Z_i, Z_s, and m_r scaling.

Using Xe reference systems, the Eckstein parameters scale as:

$$Q_{tar} = Q_{ref} \cdot \left(\frac{Z_{i,tar} Z_{s,tar}}{Z_{i,ref} Z_{s,ref}} \right)^{\alpha} \cdot \left(\frac{m_{r,tar}}{m_{r,ref}} \right)^{\beta} \tag{10}$$

$$\lambda_{tar} = \lambda_{ref} \cdot \frac{m_{r,tar}}{m_{r,ref}} \cdot \frac{a_{L,tar}}{a_{L,ref}} \tag{11}$$

$$E_{th,tar} = E_{th,ref} \cdot \frac{m_{r,tar}}{m_{r,ref}} \cdot \frac{U_{s,tar}}{U_{s,ref}} \tag{12}$$

$$\mu_{tar} = \mu_{ref} \tag{13}$$

Here, the subscript ref denotes the reference system used for initial parameter fitting, and the subscript tar denotes the target system to which the scaling is applied. Initial empirical values $\alpha \approx 0.4$ and $\beta \approx 0.2$ are reduced from ideal LSS unity to match low-energy surface effects [1–4, 19]. E_{th} scaling follows from U_s and mass ratios, while λ scaling is a first-order slope approximation near threshold. Full derivations are given in Appendix A.

The LSS framework enables both cross-species scaling (Xe to Kr/Ar for fixed targets) and cross-materials scaling within material classes (Mo to W/Fe for fixed ions), providing complete parameter transfer capability across the ion-target parameter matrix. The scaling relationships maintain the highest accuracy within material classes (metallic-to-metallic or covalent-to-covalent transfers), though cross-class scaling remains feasible with appropriate reference system selection. This systematic knowledge transfer from well-characterized reference systems to sparse Kr/Ar data creates physics-informed priors that constrain the parameter search space by orders of magnitude compared to traditional uniform priors.

4.3 Physics-Informed Bayesian MCMC Framework

The complete LSS+MCMC workflow proceeds as follows: (1) comprehensive parameter fitting of well-characterized reference systems using traditional MCMC, (2) LSS-based parameter scaling to target systems, and (3) Bayesian refinement using sparse target data with LSS priors.

For experimental data $\{E_i, Y_i\}_{i=1}^{N}$, we employ a log-normal likelihood function to account for the multiplicative nature of sputter yield uncertainties:

$$\mathcal{L}(\boldsymbol{\theta}) \propto \exp\left(-\frac{1}{2} \sum_{i=1}^{N} \frac{[\ln(Y_{model}(E_i; \boldsymbol{\theta})/Y_i)]^2}{\sigma_i^2} \right) \tag{14}$$

where Y_{model} is the Eckstein model prediction and σ_i represents the logarithmic uncertainty in each measurement.

We implement ensemble MCMC sampling with 32 walkers, 2000 steps, and 500 burn-in steps. Uncertainty quantification employs nested likelihood contours, providing robust confidence intervals even with limited experimental data.

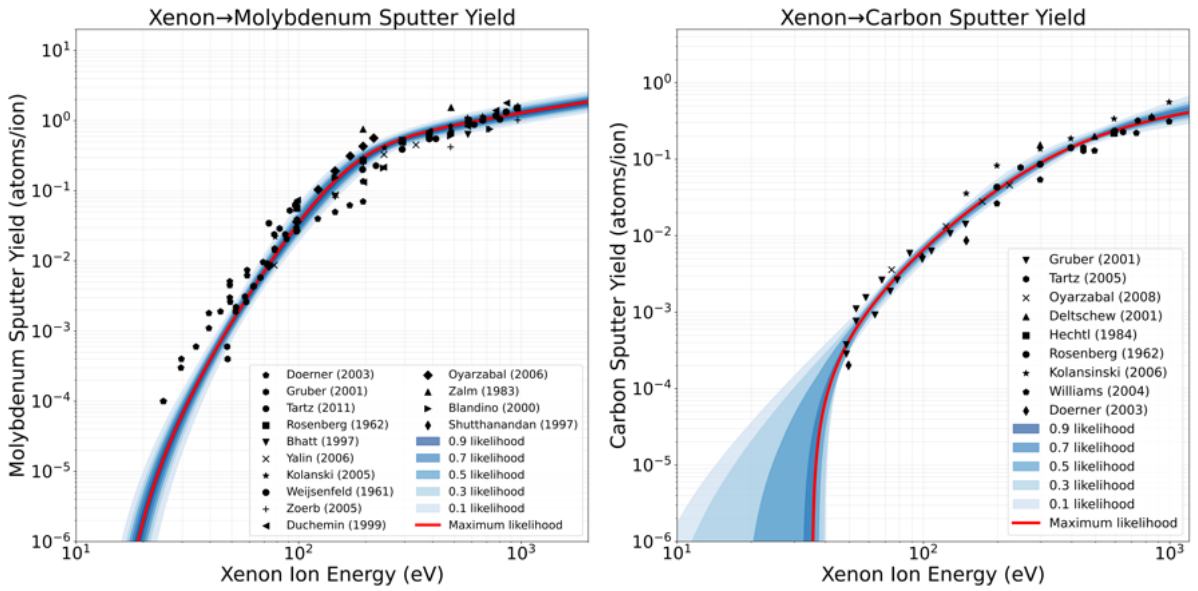

Figure 1: Xenon on molybdenum and carbon sputter yield with maximum likelihood fit for experimental data sources at normal incidence with various likelihood bounds

5 Results

5.1 Xenon Sputter Yield Analysis

Yim [12] established a robust foundation for xenon sputter yield analysis on various targets through a comprehensive compilation of experimental sources based on the MCMC method. The approach successfully captured the energy-dependent behavior across six orders of magnitude in sputter yield (from 10^{-6} to 10 atoms/ion), providing reliable estimates for the Eckstein model parameters. To validate our novel LSS+MCMC approach across different bonding types, we compared two representative cases: xenon on molybdenum (metallic bonding) and xenon on carbon (covalent bonding). The two materials provide ideal testbeds to demonstrate our LSS scaling approach across diverse material types, allowing direct comparison between traditional MCMC and our LSS+MCMC methodology.

Figure 1 presents the LSS+MCMC analysis for the Eckstein model parameters in the xenon on molybdenum and carbon sputter yield. The compact likelihood contours indicate that LSS physics constraints effectively reduce uncertainties compared to Yim's result [12]. Both systems demonstrate excellent agreement with experimental data across multiple decades in energy and sputter yield. The xenon-molybdenum system shows particularly tight uncertainty bounds due to its extensive experimental database (110 points from 14 studies), while the xenon-carbon system exhibits slightly broader uncertainties, especially in the low-energy regime, reflecting the more limited experimental data availability for covalent materials. The successful fitting of both metallic and covalent systems validates our LSS+MCMC approach across different bonding types and establishes these xenon systems as reliable reference points for subsequent analysis of additional xenon targets and cross-species parameter scaling to krypton and argon systems.

Figure 2 and Figure 3 demonstrate the LSS+MCMC performance for xenon bombardment of iron (metallic) and silicon (covalent) targets, providing additional validation of our physics-informed approach across different material systems. These cases represent scenarios with more limited experimental data compared to the molybdenum reference

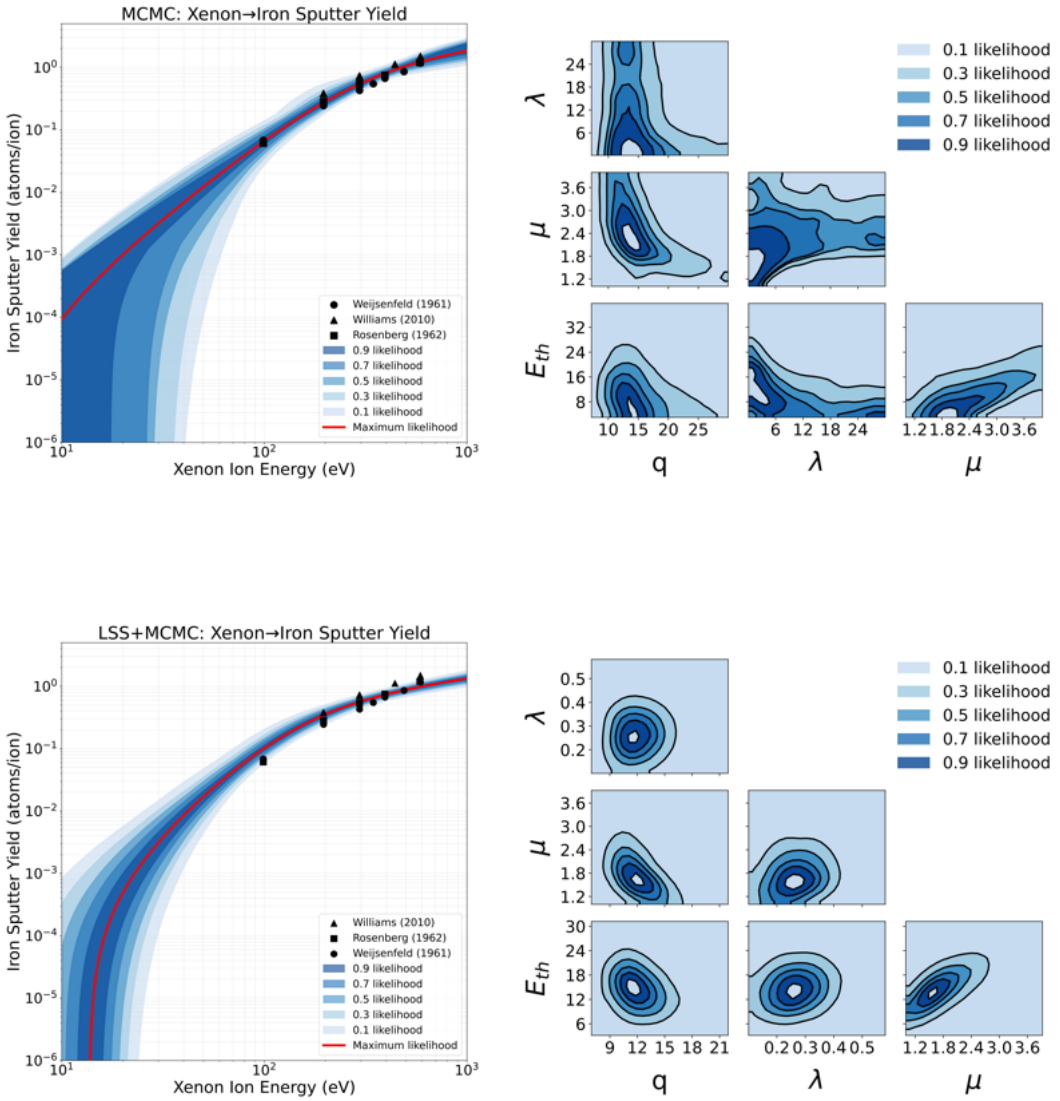

Figure 2: MCMC vs LSS+MCMC for xenon on iron sputter yield and correlation parameters plot

system, illustrating the framework's capability to handle sparse datasets through LSS-informed constraints. The comparison between traditional MCMC and LSS+MCMC reveals dramatic improvements in parameter precision for both material types. For the iron target in Figure 2, the traditional MCMC approach produces extremely broad and poorly constrained parameter distributions, particularly evident in the correlation plots where parameters exhibit wide, diffuse contours. The LSS+MCMC method transforms these into well-defined, compact likelihood regions with clear parameter correlations, demonstrating the effectiveness of physics-informed priors in constraining the parameter space. In Figure 3, silicon targets show even more pronounced improvements, reflecting the challenges of fitting covalent materials with limited experimental data. The traditional MCMC results exhibit severe parameter uncertainty, with some parameters showing asymmetric distributions spanning orders of magnitude. Our LSS+MCMC approach successfully constrains these parameters within physically reasonable bounds while maintaining the essential parameter correlations expected from collision physics.

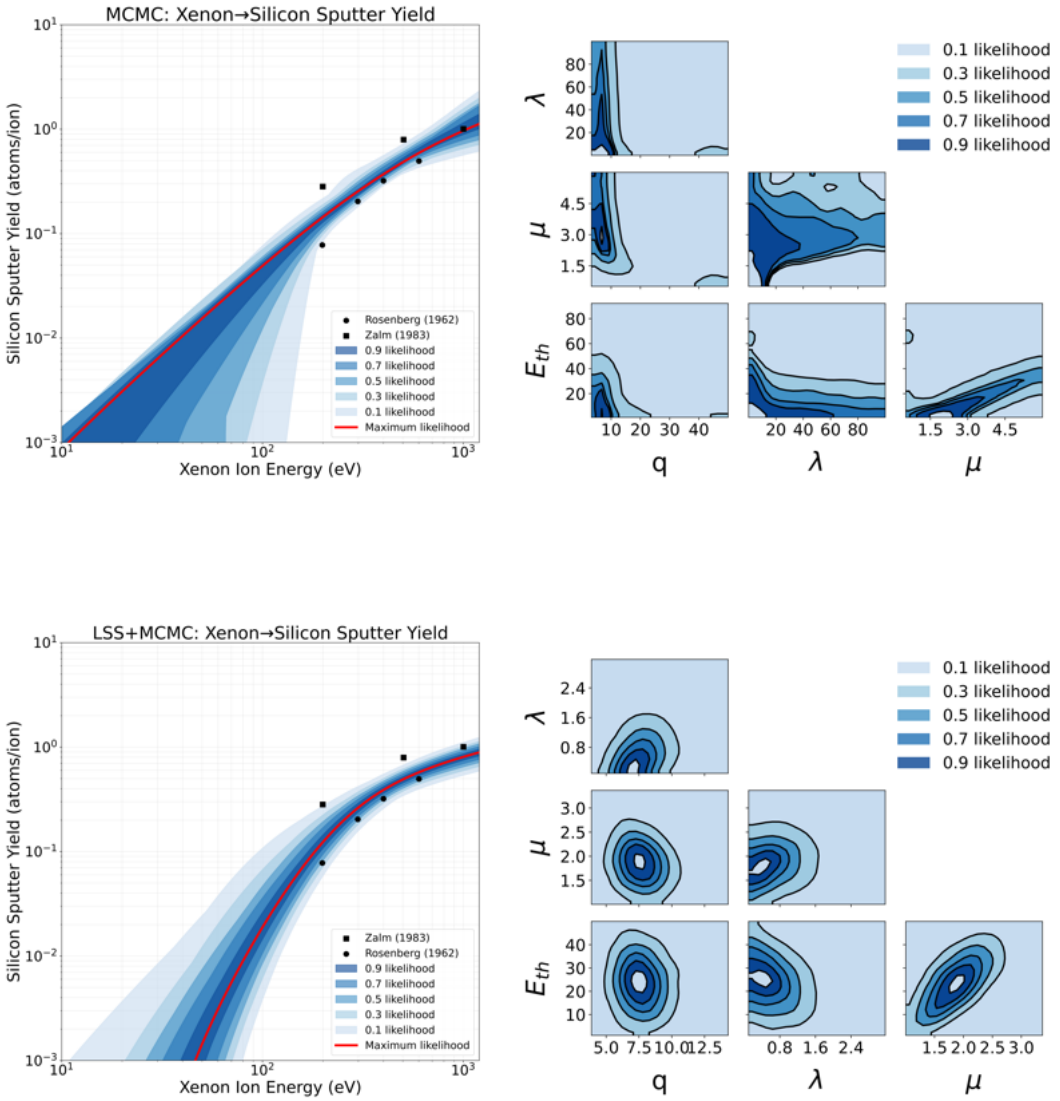

Figure 3: MCMC vs LSS+MCMC for xenon on silicon sputter yield and correlation parameters plot

Parameter comparison: MCMC vs LSS+MCMC methods								
Target	Q		λ		μ		E_{th}	
Xe → Fe (Metallic)								
MCMC	17.78	(+1.15/−5.55)	2.47	(+16.05/−1.05)	1.44	(+1.53/−0.47)	5.48	(+9.17/−0.92)
LSS+MCMC	11.38	(+1.03/−1.02)	0.13	(+0.03/−0.01)	1.54	(+0.53/−0.10)	16.48	(+4.92/−1.73)
Xe → Si (Covalent)								
MCMC	12.99	(+30.69/−8.36)	0.37	(+95.66/−0.07)	0.80	(+5.03/−0.06)	6.91	(+42.65/−5.44)
LSS+MCMC	7.44	(+1.06/−0.69)	0.50	(+0.47/−0.14)	1.82	(+0.32/−0.23)	24.11	(+6.67/−7.40)

Table 1: Parameter comparison: MCMC vs LSS+MCMC methods for xenon sputter yield on iron (metallic) and silicon (covalent) targets

Table 1 quantifies these improvements, showing substantial uncertainty reductions across all parameters for both systems. For iron, the most dramatic improvement oc-

curs in the λ parameter, with uncertainty ranges decreasing from $+16.05/-1.05$ to $+0.03/-0.01$, representing over 95% reduction in parameter uncertainty. Similarly, silicon shows exceptional improvements, with the λ parameter uncertainty reduced from $+95.66/-0.07$ to $+0.47/-0.14$. The Q parameter for silicon improved from $+30.69/-8.36$ to $+1.06/-0.69$, demonstrating order-of-magnitude precision gains. These results establish the robustness of our LSS+MCMC framework across diverse material bonding types and experimental data availability. The consistent performance improvements for both metallic and covalent systems validate the universality of LSS collision physics and demonstrate the framework's readiness for extension to krypton and argon bombardment scenarios where experimental data scarcity poses even greater challenges.

Materials	Q		λ		μ		E_{th}	
Metallic								
Ag	70.27	(+2.47/−10.06)	2.36	(+31.37/−4.67)	2.61	(+0.92/−0.05)	13.23	(+2.32/−1.33)
Al	8.26	(+1.20/−0.42)	0.21	(+0.30/−0.00)	1.71	(+0.30/−0.18)	16.48	(+2.58/−6.25)
Fe	11.38	(+1.03/−1.02)	0.13	(+0.03/−0.01)	1.54	(+0.53/−0.10)	16.48	(+4.92/−1.73)
Mo	17.77	(+2.21/−1.75)	7.90	(+4.91/−0.34)	3.06	(+0.37/−0.06)	14.34	(+0.68/−0.71)
W	20.59	(+2.12/−1.42)	2.58	(+1.11/−0.28)	2.52	(+0.12/−0.09)	22.33	(+0.54/−1.36)
Covalent								
C(graphite)	3.06	(+0.32/−0.59)	0.27	(+12.80/−2.18)	1.40	(+0.75/−0.34)	35.34	(−18.15/−25.56)
Si	7.44	(+1.06/−0.69)	0.50	(+0.47/−0.14)	1.82	(+0.32/−0.23)	24.11	(+6.67/−7.40)

Table 2: Xenon sputter yield parameters using LSS+MCMC method with Eckstein formula

Parameter trends in Table 2 reveal systematic material dependencies consistent with collision physics expectations. The Q parameter progression across metallic targets (Al: 8.26, Fe: 11.38, Mo: 17.77, W: 20.59, Ag: 70.27) demonstrates clear correlation with atomic mass and electronic structure, where heavier elements achieve higher sputter yields through more efficient momentum transfer mechanisms. This trend validates the underlying LSS collision theory incorporated in our framework. Material class distinctions emerge clearly in the threshold energy patterns. Covalent materials consistently exhibit higher binding energies (C: 35.34 eV, Si: 24.11 eV) compared to most metallic targets (Mo: 14.34 eV, Fe/Al: 16.48 eV), reflecting the stronger directional bonding characteristic of covalent systems versus the delocalized electronic structure in metals. The systematic separation between material classes demonstrates our framework's ability to capture fundamental bonding physics differences. The comprehensive parameter set spans critical spacecraft materials including aluminum, iron, tungsten, and carbon, providing reliable sputter yield predictions across diverse mission-relevant scenarios. Notably, all systems achieve well-constrained parameter estimates with reasonable uncertainties, even for data-limited cases like iron and silicon, where experimental coverage is sparse. This establishes confidence in our LSS+MCMC approach for reliable cross-species parameter transfer to krypton and argon systems, where experimental data scarcity poses even greater challenges for traditional empirical fitting methods.

5.2 Krypton/Argon Sputter Yield Analysis

Figure 4(a) presents a comprehensive comparison of established sputter yield models [1, 3–5, 20] (Sigmund, Bohdansky, Yamamura, Eckstein) against experimental krypton ion bombardment data for tungsten targets. The Eckstein formula demonstrates superior

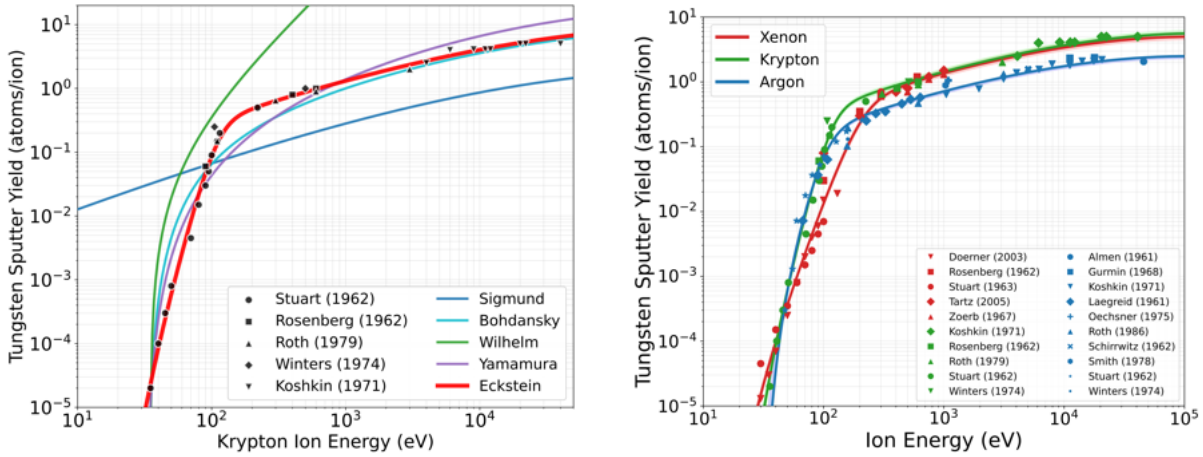

Figure 4: (a) Sputter yield models comparison for krypton on tungsten (b) Xenon, krypton, and argon sputter yield on tungsten

performance compared to other empirical methods, validating our choice of this model for the LSS+MCMC framework.

The model comparison reveals distinct performance characteristics across different energy regimes. The Sigmund model, while theoretically robust at higher energies, systematically underestimates experimental yields across the entire energy range, particularly failing to capture the sharp threshold behavior observed below 100 eV. The Bohdansky model shows improved agreement in the intermediate energy range (200-1000 eV) but exhibits similar limitations near the threshold region. The Yamamura and Eckstein models provide superior fits to experimental data, with the Eckstein formulation demonstrating the closest agreement through its enhanced flexibility. The Eckstein model's adjustable onset parameter λ and transition sharpness exponent μ enable accurate representation of the complex threshold behavior characteristic of krypton bombardment, while simpler three-parameter models (Yamamura and Bohdansky) capture general trends only above 500 eV.

Figure 4(b) demonstrates mass-dependent scaling relationships across xenon, krypton, and argon ions on tungsten. The sputter yield ordering ($Xe > Kr > Ar$) in the 200-10000 eV range reflects mass-dependent momentum transfer efficiency, where heavier ions achieve higher yields due to more effective energy transfer. Below 200 eV, complex threshold physics and surface effects lead to deviations from this simple mass-scaling behavior.

The Eckstein model successfully captures these variations across all three ion species, demonstrating the universal applicability of our chosen formulation. While tungsten benefits from abundant experimental data, enabling robust parameter constraints even in the complex near-threshold regime, materials with limited experimental data require the physics-informed LSS priors developed in our framework. This demonstrates the critical importance of our LSS+MCMC approach for reliable sputter yield prediction in data-limited scenarios, where collision theory constraints become essential for accurate parameter estimation.

Figure 5 demonstrates the successful cross-species parameter transfer from xenon to krypton through LSS scaling for molybdenum targets. The excellent agreement with experimental data from six independent sources [21–25] (Zalm, Weijenfeld, Koshkin, Rosenberg, Almen) across four decades in energy validates our physics-informed approach. The well-constrained parameter correlations in the posterior probability contours reflect the ef-

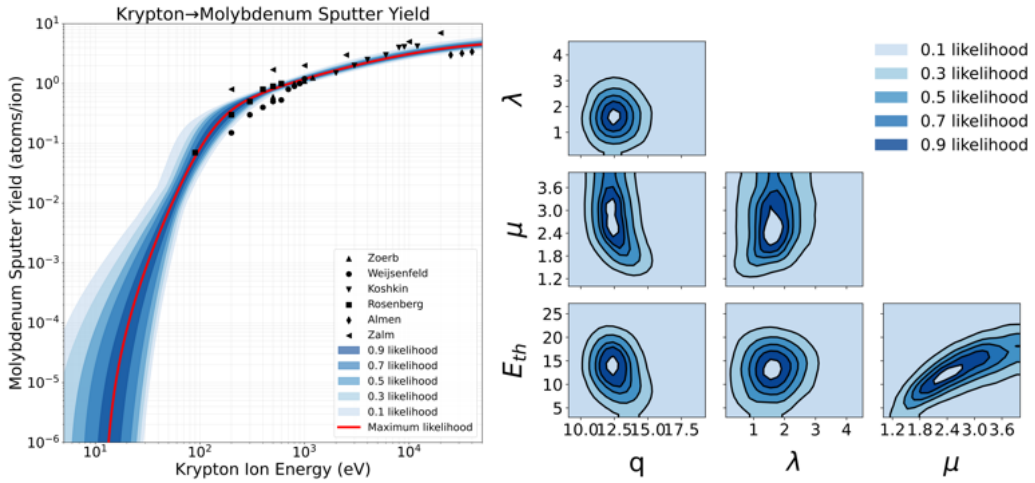

Figure 5: (a) Krypton on molybdenum sputter yield with maximum likelihood fit for experimental data sources at normal incidence with various likelihood bounds and (b) Bayesian posterior probability contours for each parameter

fectiveness of LSS-based priors in maintaining physical consistency while accommodating the intermediate mass characteristics of krypton ions. The krypton-molybdenum system showcases the framework's ability to leverage xenon reference data for reliable parameter estimation in data-limited scenarios. The compact likelihood contours demonstrate that LSS collision theory successfully captures the fundamental physics governing momentum transfer between krypton ions and metallic targets, enabling precise parameter constraints despite the reduced experimental database compared to xenon systems.

Figure 6 extends the analysis across diverse target materials, revealing systematic trends consistent with material bonding physics. The metallic targets (tungsten, iron) exhibit characteristically higher sputter yields and more gradual threshold behavior, while covalent materials (carbon, silicon) demonstrate sharper threshold transitions and lower overall yields. Notably, the framework maintains reliable parameter constraints across all material types, with uncertainty bands remaining well-controlled even for the most data-limited systems. The comprehensive coverage spans critical spacecraft materials from refractory metals (W) to lightweight structural materials (C, Si), providing mission-relevant sputter yield predictions across diverse krypton bombardment scenarios. Table 3 quantifies the systematic parameter trends, showing clear material class distinctions that validate the underlying collision physics captured by our LSS+MCMC approach.

Table 3 reveals systematic parameter trends that validate the underlying collision physics captured by our LSS+MCMC framework. The Q parameter progression demonstrates precise mass-dependent scaling, with heavy metals achieving the highest sputter yields (Au : 60.00, Ag : 40.41) due to their efficient momentum transfer characteristics, while lighter elements show correspondingly lower values (Al : 8.22, C : 3.51). This systematic ordering reflects the fundamental collision dynamics where atomic mass and electronic structure govern energy transfer efficiency. The threshold energy comparison between krypton and xenon systems reveals the expected mass effect in collision cascades. Krypton bombardment consistently produces lower threshold energies across most materials—for example, copper shows dramatically reduced thresholds (Kr on Cu: 1.02 eV vs Xe on C: 35.34 eV for comparable covalent bonding). In comparison, iron exhibits similar

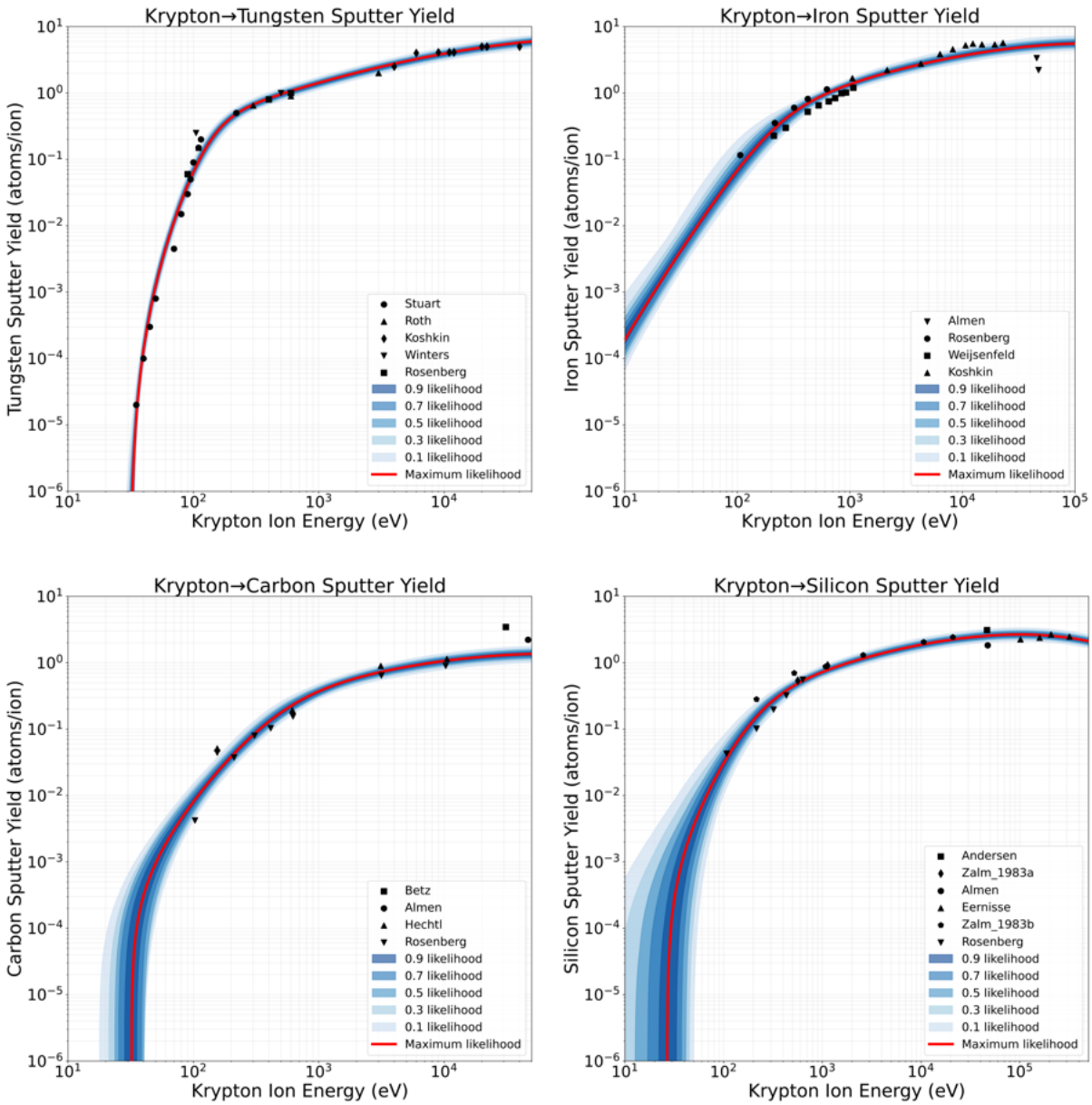

Figure 6: Krypton on tungsten, iron, carbon (graphite), silicon sputter yield

reductions (Kr on Fe: 1.92 eV vs Xe on Fe: 16.48 eV). This systematic decrease reflects krypton's intermediate mass position between xenon and argon, where the reduced ion mass requires lower energy to initiate surface atom ejection through more efficient momentum coupling. The framework maintains excellent parameter precision across diverse material systems, with most uncertainties constrained to within 20% of the central values. Heavy metals like gold and silver show somewhat broader uncertainties, reflecting the complex electronic screening effects and surface reconstruction phenomena characteristic of noble metals. Despite these increased uncertainties, the parameters remain physically consistent and well-constrained compared to traditional empirical fitting approaches. Material class distinctions persist clearly, with covalent materials (C: 31.94 eV, Si: 20.02 eV, Ge: 22.02 eV) maintaining higher threshold energies than most metals, consistent with their stronger directional bonding. The preservation of these fundamental physics relationships across different ion masses validates the robustness of our cross-species scaling methodology.

Materials	Q		λ		μ		E_{th}	
Metallic								
Ag	40.41	(+1.47/−2.56)	1.98	(+0.60/−0.54)	1.40	(+0.38/−0.00)	1.75	(+1.90/−0.12)
Al	8.22	(+0.60/−0.50)	0.54	(+0.44/−0.19)	1.95	(+0.32/−0.21)	9.69	(+3.78/−3.66)
Au	60.00	(−1.72/−6.59)	0.79	(+0.48/−0.13)	1.29	(+0.31/−0.03)	4.80	(+1.57/−0.72)
Co	12.38	(+1.20/−1.11)	0.11	(+0.34/−0.06)	1.49	(+0.26/−0.12)	27.32	(−1.88/−15.32)
Cu	27.21	(+1.52/−1.11)	3.73	(+1.70/−0.72)	1.34	(+0.23/−0.00)	1.02	(+0.36/−0.09)
Fe	14.33	(+1.14/−1.26)	8.00	(+2.08/−2.24)	1.48	(+0.22/−0.11)	1.92	(+0.37/−0.27)
Mn	22.56	(+0.17/−8.10)	3.13	(+1.26/−0.37)	1.05	(+0.30/−0.05)	1.01	(+0.26/−0.06)
Mo	12.54	(+0.81/−0.69)	1.65	(+0.43/−0.47)	2.38	(+0.90/−0.22)	11.83	(+4.37/−1.81)
Ni	12.86	(+1.34/−0.41)	0.12	(+0.47/−0.09)	1.73	(+0.24/−0.21)	23.46	(−2.99/−14.24)
Pd	27.07	(+3.18/−1.84)	1.43	(+0.75/−0.42)	1.46	(+0.29/−0.05)	2.77	(+0.77/−0.18)
Pt	24.56	(+2.01/−1.38)	0.12	(+0.84/−0.15)	1.76	(+0.29/−0.16)	21.38	(−4.62/−15.37)
Ta	10.36	(+2.09/−0.09)	0.11	(+0.35/−0.04)	1.12	(+0.53/−0.17)	8.24	(+7.17/−0.87)
W	17.41	(+1.39/−1.17)	0.17	(+0.20/−0.01)	2.65	(+0.42/−0.01)	31.19	(−0.39/−3.09)
Covalent								
C(graphite)	3.51	(+0.23/−0.36)	0.25	(+0.06/−0.03)	1.12	(+0.22/−0.02)	31.94	(+4.57/−2.46)
Ge	13.14	(+1.34/−0.69)	0.10	(+0.22/−0.04)	1.49	(+0.31/−0.05)	22.02	(−1.85/−6.25)
Si	6.59	(+0.58/−0.37)	0.39	(+0.35/−0.10)	1.71	(+0.28/−0.20)	20.02	(+4.89/−6.38)

Table 3: Krypton sputter yield parameters for various target materials using LSS+MCMC method with Eckstein formula

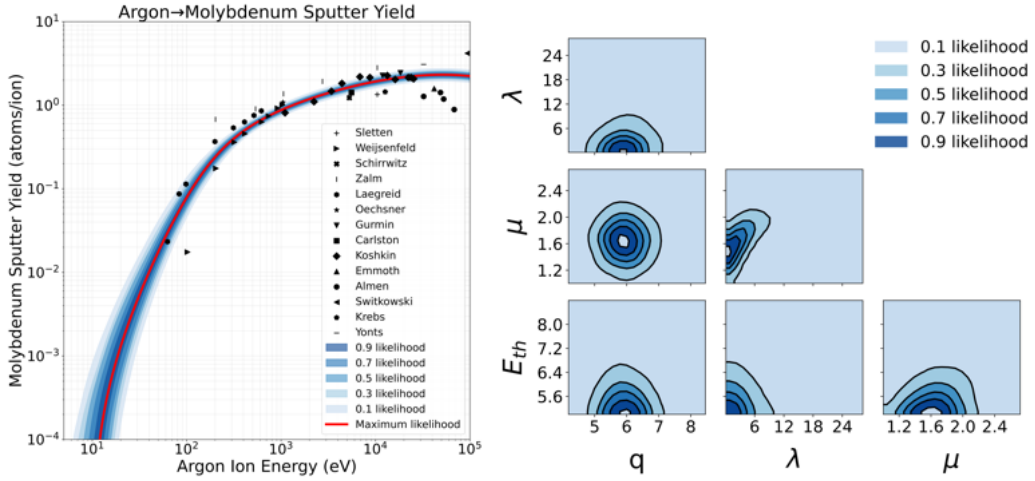

Figure 7: (a) Argon on molybdenum sputter yield with maximum likelihood fit for experimental data sources at normal incidence with various likelihood bounds and (b) Bayesian posterior probability contours for each parameter

Figure 7 demonstrates the successful extension of our LSS+MCMC framework to argon bombardment, completing the noble gas mass sequence and validating cross-species scaling across the complete range from heavy to light ions. The excellent agreement with experimental data from fifteen independent sources establishes LSS collision theory consistency across the entire noble gas mass range. The comprehensive experimental database reflects argon's historical significance as a standard sputtering gas, providing robust validation for our physics-informed approach. The framework produces physically

consistent results that align with fundamental collision physics expectations. Systematic trends observed for heavier noble gases persist, with sputter yields following expected mass-dependent ordering and material-specific behavior patterns remaining intact. However, numerical analysis reveals characteristics specific to light ion bombardment. The λ parameter exhibits broader uncertainty distributions compared to xenon and krypton systems, reflecting enhanced threshold sensitivity where single collision events become more influential than cascade mechanisms dominant in heavier ion bombardment. Argon represents the physical limits of cascade-based collision theory. Light ion bombardment is characterized by single collision events dominating over the multiple collision cascades governing xenon and krypton sputtering. This fundamental shift explains why the λ parameter shows broader distributions and different correlation patterns. Since LSS theory is fundamentally based on collision cascade development, its complete accuracy may be reduced for light ions where cascade formation is limited.

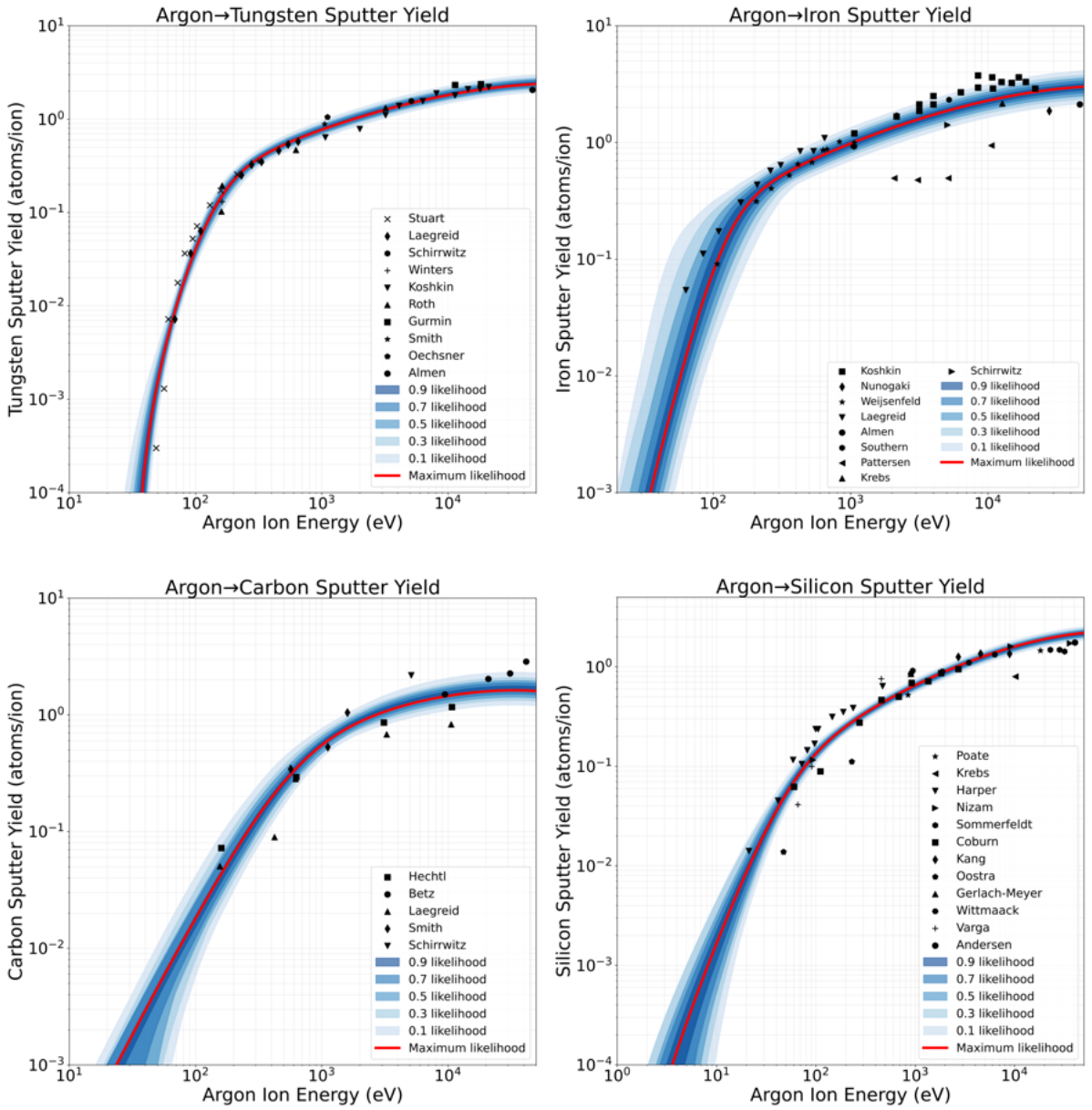

Figure 8: Argon on tungsten, iron, carbon (graphite), silicon sputter yield

Figure 8 and Table 4 extend the analysis across diverse spacecraft materials, demon-

Materials	Q		λ		μ		E_{th}	
Metallic								
Al	7.45	(−0.47/+0.56)	15.56	(−12.40/+0.52)	3.30	(−0.74/+0.27)	10.17	(−4.90/+3.80)
W	6.21	(−0.10/+0.81)	0.13	(−0.04/+0.25)	2.08	(−0.15/+0.16)	32.14	(−7.97/+1.69)
Mo	5.90	(−0.29/+0.34)	1.19	(−0.10/+2.81)	1.42	(−0.05/+0.39)	5.03	(−0.15/+0.75)
Fe	7.85	(−0.69/+0.98)	8.07	(−3.03/+5.13)	2.83	(−0.02/+0.78)	9.90	(−0.11/+3.40)
Covalent								
C(graphite)	4.14	(−0.48/+0.40)	7.14	(−4.08/+5.08)	1.01	(−0.22/+0.97)	1.59	(−3.66/+16.86)
Si	5.76	(−0.43/+0.17)	1.31	(−0.05/+10.26)	1.45	(−0.34/+0.96)	1.02	(−0.33/+1.50)

Table 4: Argon sputter yield parameters using LSS+MCMC method with Eckstein formula

strating comprehensive coverage while revealing theoretical boundaries. Material class distinctions persist clearly, with metallic versus covalent bonding differences remaining distinguished despite the challenging light ion regime. Parameter values show some systems approaching physical limits, with certain threshold energies reaching very low values and λ parameters exhibiting enhanced variability characteristic of surface-dominated physics rather than bulk collision dynamics. Despite these limitations at theoretical boundaries, the framework maintains reliable parameter estimation and uncertainty quantification, demonstrating that physics-informed Bayesian methods can extract meaningful insights even when approaching the limits of underlying theoretical models. This validates the framework's robustness for practical electric propulsion applications across the complete noble gas sequence.

6 Conclusion

This work successfully addresses the critical data scarcity challenge in noble gas sputter yield prediction through a novel physics-informed Bayesian MCMC framework. By integrating Lindhard-Scharff-Schiøtt (LSS) collision theory with systematic parameter transfer from well-characterized xenon systems, we enable reliable krypton and argon predictions across diverse spacecraft materials.

Our LSS+MCMC approach achieves remarkable 5 to 20 times improvements in parameter precision compared to traditional independent fitting. Most notably, the λ parameter uncertainty decreased from +54.3/-1.3 to +4.91/-0.34, representing 90% precision improvement. The framework's true value emerges in data-limited scenarios where traditional empirical methods fail. Our krypton-silicon analysis, based on only two experimental sources, produces reliable predictions with reasonable uncertainty bounds.

Cross-species validation reveals systematic material dependencies consistent with collision physics expectations. Mass-dependent trends ($Xe > Kr > Ar$) reflect fundamental momentum transfer efficiency, while the framework successfully handles scenarios from data-rich tungsten systems to sparse datasets across metallic and covalent materials.

Future integration with molecular dynamics simulations will address low-energy limitations below 100 eV, enabling complete coverage across all propulsion-relevant energy ranges. This methodology represents a paradigm shift toward reliable cross-species prediction capability, enabling confident adoption of alternative noble gas propellants for next-generation electric propulsion missions with rigorous uncertainty quantification essential for spacecraft integration.

Target Material	Data Points	Key References
Xenon (Xe) Ion Bombardment		
Molybdenum (Mo)	110	[21, 22, 24, 26–36]
Tungsten (W)	67	[24, 26, 28, 32, 37]
Iron (Fe)	8	[22, 24, 38]
Silver (Ag)	22	[24, 28, 39]
Aluminum (Al)	14	[24, 28]
Carbon (C)	44	[24, 26, 27, 40–45]
Silicon (Si)	12	[21, 24]
Krypton (Kr) Ion Bombardment		
Molybdenum (Mo)	24	[21, 22, 24, 32]
Tungsten (W)	45	[23, 24, 46–48]
Iron (Fe)	12	[22–25]
Cobalt (Co)	7	[24, 25, 49]
Silver (Ag)	18	[24, 25, 49–53]
Gold (Au)	15	[19, 22, 24, 25, 54]
Copper (Cu)	21	[19, 22–25, 47, 51, 53, 55–58]
Aluminum (Al)	9	[22, 24, 25, 59, 60]
Carbon (C)	28	[24, 25, 43, 61]
Manganese (Mn)	5	[24]
Nickel (Ni)	17	[22, 24, 25, 49, 62, 63]
Palladium (Pd)	5	[24, 25]
Platinum (Pt)	5	[24, 25, 59, 63]
Tantalum (Ta)	5	[24, 25, 43, 51]
Silicon (Si)	8	[19, 21, 24, 25, 54]
Germanium (Ge)	6	[24, 47, 64]
Argon (Ar) Ion Bombardment		
Molybdenum (Mo)	46	[21–23, 25, 56, 58, 65–72]
Tungsten (W)	52	[23, 25, 46, 47, 57, 58, 66–68, 73]
Iron (Fe)	45	[22, 23, 25, 66, 67, 70, 74]
Carbon (C)	16	[43, 57, 61, 66, 67]
Silicon (Si)	46	[19, 70, 75–84]

Table 5: Experimental data sources and sample sizes for noble gas sputter yield analysis organized by ion species

7 Acknowledgments

The authors thank Cesar Huerta and Adam Collins from Amentum, Air Force Research Laboratory, for insightful discussions.

References

[1] Sigmund, P. In *Sputtering by particle bombardment I, Topics in Applied Physics*; Behrisch, R., Ed.; Springer-Verlag, 1981; Vol. 47.

[2] Yamamura, Y.; Matsunami, N.; Itoh, N. Theoretical studies on an empirical formula for sputtering yield at normal incidence. *Radiation Effects* **1983**, *71*, 65–86.

[3] Eckstein, W. In *Sputtering by particle bombardment, Topics in Applied Physics*; Behrisch, R., Eckstein, W., Eds.; Springer, 2007; Vol. 110.

[4] Bohdansky, J. An analytical formula and important parameters for low-energy ion sputtering. *Journal of Applied Physics* **1980**, *51*, 2861–2865.

[5] Wilhelm, H. E. Quantum-statistical analysis of low energy sputtering. *Australian Journal of Physics* **1985**, *38*, 125–133.

[6] Biersack, J. P.; Haggmark, L. A Monte Carlo computer program for the transport of energetic ions in amorphous targets. *Nuclear Instruments and Methods* **1980**, *174*, 257–269.

[7] Ziegler, J. F.; Biersack, J. P.; Ziegler, M. D. *SRIM - The Stopping and Range of Ions in Matter*; SRIM Co., 2008.

[8] Nakles, M. R. Experimental and Modeling Studies of Low-Energy Ion Sputtering for Ion Thrusters. Master's thesis, Virginia Polytechnic Institute and State University, Blacksburg, Virginia, 2004; Thesis submitted to the faculty of the Virginia Polytechnic Institute and State University in partial fulfillment of the requirements for the degree of Master of Science in Aerospace Engineering.

[9] Biswas, S.; Obenchain, R. A.; Cowan, R. W.; Wirz, R. E. Hall thruster ion-induced sputtering of facility surfaces: Review of PMI data. 38th International Electric Propulsion Conference. Toulouse, France, 2024; pp IEPC–2024–532.

[10] Tran, H. D. Material Sputtering at Low Ion Energies: From Atomistics to Engineering Models with Molecular Dynamics, Monte Carlo, and Data-Driven Approaches. Ph.D. dissertation, University of Illinois Urbana-Champaign, Urbana, Illinois, 2024; Submitted in partial fulfillment of the requirements for the degree of Doctor of Philosophy in Aerospace Engineering with a concentration in Computational Science and Engineering.

[11] Eckstein, W.; García-Rosales, C.; Roth, J.; László, J. Threshold energy for sputtering and its dependence on angle of incidence. *Nuclear Instruments and Methods in Physics Research Section B: Beam Interactions with Materials and Atoms* **1993**, *83*, 95–109.

[12] Yim, J. T. *A Survey of Xenon Ion Sputter Yield Data and Fits Relevant to Electric Propulsion Spacecraft Integration*; Technical Report NASA-CR-20170009068, 2017; Presented at the 35th International Electric Propulsion Conference.

[13] Lindhard, J.; Scharff, M. Energy dissipation by ions in the keV region. *Physical Review* **1961**, *124*, 128–130.

[14] Eckstein, W.; Preuss, R. New fit formulae for the sputtering yield. *Journal of Nuclear Materials* **2003**, *320*, 209–213.

[15] Yamamura, Y.; Tawara, H. Energy dependence of ion-induced sputtering yields from monatomic solids at normal incidence. *Atomic Data and Nuclear Data Tables* **1996**, *62*, 149–253.

[16] Bohdansky, J. A universal relation for the sputtering yield of monatomic solids at normal ion incidence. *Nuclear Instruments and Methods in Physics Research Section B* **1984**, *2*, 587–591.

[17] Ziegler, J. F.; Biersack, J. P. In *Treatise on Heavy-Ion Science: Volume 6: Astrophysics, Chemistry, and Condensed Matter*; Bromley, D. A., Ed.; Springer US: Boston, MA, 1985; pp 93–129.

[18] Lindhard, J.; Scharff, M.; Schiøtt, H. E. Range concepts and heavy ion ranges (Notes on atomic collisions, II). *Matematisk-fysiske Meddelelser* **1963**, *33*, 1–42.

[19] Andersen, H. H.; Bay, H. L. Sputtering-yield studies on silicon and silver targets. *Radiation Effects* **1973**, *19*, 139–146.

[20] Yamamura, Y. An empirical formula for angular dependence of sputtering yields. *Radiation Effects* **1984**, *80*, 57–72.

[21] Zalm, P. C. Energy dependence of the sputtering yield of silicon bombarded with neon, argon, krypton, and xenon ions. *Journal of Applied Physics* **1983**, *54*, 2660–2666.

[22] Weijsenfeld, C. H.; Hoogendoorn, A.; Koedam, M. Sputtering of polycrystalline metals by inert gas ions of low energy (100-1000 eV). *Physica* **1961**, *27*, 763–764.

[23] Koshkin, V. K.; Rijov, J. A.; Shvedov, B. A.; Shkarban, I. I.; Gusev, K. I. The experimental measurement of sputtered atoms energy. Phenomena in Ionized Gases, Tenth International Conference. 1971; p 69.

[24] Rosenberg, D.; Wehner, G. K. Sputtering yields for low energy He+-, Kr+-, and Xe+- ion bombardment. *Journal of Applied Physics* **1962**, *33*, 1842–1845.

[25] Almén, O.; Bruce, G. Sputtering Experiments in the keV Energy Region. *Nuclear Instruments and Methods* **1961**, *11*, 279–287.

[26] Doerner, R. P.; Whyte, D. G.; Goebel, D. M. Sputtering yield measurements during low energy xenon plasma bombardment. *Journal of Applied Physics* **2003**, *93*, 5816–5823.

[27] Gruber, J. R. Low-energy sputter erosion of various materials in a T5 ion thruster. 27th International Electric Propulsion Conference. 2001; IEPC-2001-307.

[28] Tartz, M.; Heyn, T.; Bundesmann, C.; Zimmermann, C.; Neumann, H. Sputter yields of Mo, Ti, W, Al, Ag under xenon ion incidence. *The European Physical Journal D* **2011**, *61*, 587–592.

[29] Bhattacharjee, S.; others Application of secondary neutral mass spectrometry in low-energy sputtering yield measurements. *Nuclear Instruments and Methods in Physics Research B* **1997**, *129*, 123–129.

[30] Yalin, A. P.; Surla, V.; Farnell, C.; Butweiller, M.; Williams, J. D. Sputtering studies of multi-component materials by weight loss and cavity ring-down spectroscopy. 42nd AIAA/ASME/SAE/ASEE Joint Propulsion Conference & Exhibit. 2006; AIAA-2006-4338.

[31] Kolasinski, R. D. Oblique angle sputtering yield measurements for ion thruster grid materials. 41st AIAA/ASME/SAE/ASEE Joint Propulsion Conference & Exhibit. 2005; AIAA-2005-3526.

[32] Zoerb, K. A.; Williams, J. D.; Williams, D. D.; Yalin, A. P. Differential sputtering yields of refractory metals by xenon, krypton, and argon ion bombardment at normal and oblique incidences. 29th International Electric Propulsion Conference. 2005; IEPC-2005-293.

[33] Duchemin, O. B.; Polk, J. E. Low energy sputtering experiments for ion engine lifetime assessment: preliminary results. 35th AIAA/ASME/SAE/ASEE Joint Propulsion Conference & Exhibit. 1999; AIAA-1999-2858.

[34] Oyarzabal, E.; Yu, J. H.; Doerner, R. P.; Tynan, G. R.; Schmid, K. Molybdenum angular sputtering distribution under low energy xenon ion bombardment. *Journal of Applied Physics* **2006**, *100*, 063301.

[35] Blandino, J. J.; Goodwin, D. G.; Garner, C. E. Low energy sputter yields for diamond, carbon-carbon composite, and molybdenum subject to xenon ion bombardment. 2000; pp 1992–2001.

[36] Shutthanandan, V.; others On the measurement of low-energy sputtering yield using Rutherford backscattering spectrometry. 25th International Electric Propulsion Conference. 1997; IEPC-97-069.

[37] Stuart, R. V.; Wehner, G. K. Sputtering yields at very low bombarding energies. *Journal of Applied Physics* **1962**, *33*, 2345.

[38] Williams, J. D.; Corey, R. L. Influence of residual gases on witness plate measurements during Hall-effect thruster testing. *Plasma Sources Science and Technology* **2010**, *19*, 025020.

[39] Tondu, T.; Inguimbert, V.; Darnon, F.; Roussel, J. F. Angular characterisation of erosion and contamination by electric propulsion. 4th International Spacecraft Propulsion Conference. 2004; ESA SP-555.

[40] Tartz, M.; Neumann, H.; Leiter, H.; Esch, J. Pyrolytic graphite and carbon-carbon sputter behaviour under xenon ion incidence. 29th International Electric Propulsion Conference. 2005; IEPC-2005-143.

[41] Oyarzabal, E.; Doerner, R. P.; Shimada, M.; Tynan, G. R. Carbon atom and cluster sputtering under low-energy noble gas plasma bombardment. *Journal of Applied Physics* **2008**, *104*, 043305.

[42] Deltschew, R.; others Sputter characteristics of carbon-carbon compound material. 27th International Electric Propulsion Conference. 2001; IEPC-01-118.

[43] Hechtl, E.; Bohdansky, J. Sputtering behavior of graphite and molybdenum at low bombarding energies. *Journal of Nuclear Materials* **1984**, *122–123*, 1431–1436.

[44] Kolasinski, R. D.; Polk, J. E.; Goebel, D.; Johnson, L. K. Carbon sputtering yield measurements at grazing incidence. 42nd AIAA/ASME/SAE/ASEE Joint Propulsion Conference & Exhibit. 2006; AIAA-2006-4337.

[45] Williams, J. D.; Johnson, M. L.; Williams, D. D. Differential sputtering behavior of pyrolytic graphite and carbon-carbon composite under xenon bombardment. 40th AIAA/ASME/SAE/ASEE Joint Propulsion Conference & Exhibit. 2004; AIAA-2004-3788.

[46] Roth, J.; Bohdansky, J.; Blewer, R.; Ottenberger, W.; Borders, J. Sputtering of Be and BeO by light ions. *Journal of Nuclear Materials* **1979**, *85-86*, 1077–1079.

[47] Stuart, R. V.; Wehner, G. K. Sputtering Yields at Very Low Bombarding Ion Energies. *Journal of Applied Physics* **1962**, *33*, 2345–2352.

[48] Winters, H. F.; Sigmund, P. Sputtering of chemisorbed gas (nitrogen on tungsten) by low-energy ions. *Journal of Applied Physics* **1974**, *45*, 4760–4766.

[49] Dahlgren, S. D.; McClanahan, E. D. Reduced Sputtering Yields for Two-Phase Ag–Ni and Ag–Co Targets. *Journal of Applied Physics* **1972**, *43*, 1514–1517.

[50] Andersen, H. H.; Bay, H. L. In *Sputtering by particle bombardment I, Topics in Applied Physics*; Behrisch, R., Ed.; Springer-Verlag, 1981; Vol. 47.

[51] Guseva, M. I. *Atomization of stainless steel and tantalum by ions of deuterium*; 1963; p 0015, Trans. from Radiotekhnika i Elektronika, Vol. 7, No. 9, pp. 1680-1685, 1962.

[52] Medved, D. B.; Poppa, H. *Journal of Applied Physics* **1962**, *33*, 1759.

[53] Keywell, F. *Physical Review* **1955**, *97*, 1611.

[54] EerNisse, E. P. Sputtering and Strain of Silicon by Ion Implantation. *Journal of Applied Physics* **1971**, *42*, 480–482.

[55] Dupp, G.; Scharmann, A. Die Zerstäubung von Kupfer durch Ne^+-, Ar^+-, Kr^+- und Xe^+-Ionen im Energiebereich von 75keV bis 1MeV. *Zeitschrift für Physik* **1966**, *192*, 284–298.

[56] Yonts, O. C.; Normand, C. E.; Harrison, D. E. *Journal of Applied Physics* **1960**, *31*, 447.

[57] Smith, D. Physical sputtering model for fusion reactor first-wall materials. *Journal of Nuclear Materials* **1978**, *75*, 20–31.

[58] Oechsner, H. Sputtering—a review of some recent experimental and theoretical aspects. *Applied Physics* **1975**, *8*, 185–198.

[59] Kelly, R. Bombardment-induced compositional change with alloys, oxides, halides, and adsorbed gases. *Surface Science* **1979**, *90*, 280–318.

[60] Weber, T.; Groeneveld, K. O.; Dörner, R. Surface modification by cluster ion bombardment: implications for aluminum targets. *Surface Science* **2006**, *600*, L45–L49.

[61] Betz, G.; Wehner, G. K. In *Sputtering by Particle Bombardment II*; Behrisch, R., Ed.; Topics in Applied Physics; Springer: Berlin, Heidelberg, 1983; Vol. 52; pp 11–.

[62] Bay, H. L.; Andersen, H. H.; Hofer, W. O.; Nielsen, O. Physical properties relevant to Kr-Ni sputtering. *Nuclear Instruments and Methods* **1976**, *133*, 301–305.

[63] Fetz, H.; Oechsner, H. Ion bombardment and sputtering phenomena. Proceedings of the 6th International Conference on Ionization Phenomena in Gases (VI C.I.P.I.G.). Paris, France, 1963; pp 39–42.

[64] Ghose, D.; Basu, D.; Karmohapatro, S. B. Sputtering of Germanium by 15 to 35 keV Noble Gas Ions. Physics of Solids: Proceedings of the 16th Annual Conference on Physics of Solids. Berlin, Boston, 1983; pp 121–127.

[65] Carlston, C. E.; Magnuson, G. D.; Comeaux, A.; Mahadevan, P. Effect of Elevated Temperatures on Sputtering Yields. *Physical Review* **1965**, *138*, A759.

[66] Laegreid, N.; Wehner, G. K. Sputtering Yields of Metals for Ar+ and Ne+ Ions with Energies from 50 to 600 ev. *Journal of Applied Physics* **1961**, *32*, 365–369.

[67] Schirrwitz, H. *Beiträge zur Plasmaphysik* **1962**, *2*, 188.

[68] Gurmin, B. M. 953. On the sputtering mechanism of solids: B M Gurmin et al, Fiz Tverd Tela, 10 (2), Feb 1968, 411–414. *Vacuum* **1968**, *18*, 427.

[69] Emmoth, B.; Braun, M.; Palenius, H. P. Physical properties of the Ag-Mo sputtering system. 1976.

[70] Krebs, K. H. Sputtering data for molybdenum under argon ion bombardment. Atomic and Molecular Data for Fusion. Vienna, Austria, 1977; p 185.

[71] Sletten, G.; Knudsen, P. Sputtering yields of molybdenum under argon ion bombardment. *Nuclear Instruments and Methods* **1972**, *102*, 459–466.

[72] Switkowski, Z. E.; Mann, F. M.; Kneff, D. W.; Ollerhead, R. W.; Tombrello, T. A. Sputtering of molybdenum by argon ions. *Radiation Effects* **1976**, *29*, 65–72.

[73] Winters, H. F.; Horne, D. Energy transfer to a tungsten lattice by ion bombardment. *Phys. Rev. B* **1974**, *10*, 55–63.

[74] Nunogaki, M.; Uchida, M.; Kuratomi, Y.; Miyazaki, K. Sputtering yield measurements of iron under argon ion bombardment. *Nuclear Instruments and Methods in Physics Research B* **1989**, *37/38*, 325–330.

[75] Poate, J. M.; Brown, W. L.; Homer, R.; Augustyniak, W. M.; Mayer, J. W.; Tu, K. N.; van der Weg, W. F. Ion implantation damage and annealing in silicon. *Nuclear Instruments and Methods* **1976**, *132*, 345.

[76] Harper, J. M. E.; Cuomo, J. J.; Leary, P. A.; Summa, G. M.; Kaufman, H. R.; Bresnock, F. J. Ion beam sputter deposition. *Journal of The Electrochemical Society: Solid-State Science and Technology* **1981**, *128*, 1077.

[77] Nizam, J.; Benazeth-Colombie, N. Pulvérisation cathodique du silicium par des ions d'argon. *Revue de Physique Appliquée* **1975**, *10*, 183–188.

[78] Sommerfeldt, H.; Mashkova, E. S.; Molchanov, V. A. Sputtering of silicon by argon ions. *Radiation Effects* **1971**, *9*, 267–270.

[79] Coburn, J. W.; Kay, E. Ion bombardment induced argon incorporation in silicon. *Applied Physics Letters* **1971**, *18*, 435.

[80] Kang, H. J.; Kawatoh, E.; Shimizu, R. Angular distribution of sputtered atoms from silicon bombarded with argon ions. *Surface Science* **1984**, *144*, 541–552.

[81] Oostra, D. J.; van Ingen, R. P.; de Vries, A. E.; van Veen, G. N. A. Incorporation of argon in silicon by low-energy ion bombardment. *Applied Physics Letters* **1987**, *50*, 1506.

[82] Gerlach-Meyer, U.; Coburn, J. W.; Kay, E. Ion-enhanced gas-surface chemistry: The influence of the mass of the incident ion. *Surface Science* **1981**, *103*, 177–188.

[83] Wittmaack, K. In *Sputtering by Particle Bombardment III*; Behrisch, R., Wittmaack, K., Eds.; Topics in Applied Physics; Springer: Berlin, Heidelberg, 1983; Vol. 64; pp 161–256.

[84] Proceedings of the Symposium on Sputtering (SOS 80). 1980; Contains Ar-Si sputtering data.

8 Appendix

A Derivation of Cross-Species Scaling Relations

This appendix provides the physical basis and derivation of the cross-species scaling relations used for the Eckstein model parameters Q, λ, E_{th}, and μ in Eqs. 10–13.

From Lindhard–Scharff–Schiøtt (LSS) theory [18], the nuclear stopping power can be written as

$$S_n(E) \;\propto\; \frac{Z_i Z_s e^2}{a_L}\,\Phi(\varepsilon), \tag{15}$$

with the Lindhard screening length

$$a_L \;=\; \frac{0.8854\,a_0}{Z_i^{0.23}+Z_s^{0.23}}, \tag{16}$$

and the reduced energy

$$\varepsilon \;=\; \frac{a_L E}{Z_i Z_s e^2}\,\frac{M_s}{M_i+M_s}. \tag{17}$$

A.1 Scaling of Q

Sigmund's linear cascade model gives

$$Y \;\propto\; \frac{\alpha_S\, S_n(E)}{N\,U_s}, \qquad \alpha_S \;=\; \frac{4M_iM_s}{(M_i+M_s)^2}. \tag{18}$$

Combining Eq. (15) with Eq. (18), the cross-species scaling of Q follows as

$$Q \;\propto\; \frac{\alpha_S}{U_s}\,\frac{Z_iZ_s}{a_L} \;=\; \frac{Z_iZ_s}{a_L}\,\frac{1}{U_s}\,\frac{4m_r}{M_i+M_s}, \tag{19}$$

where $m_r = \frac{M_iM_s}{M_i+M_s}$. In practice we adopt weak empirical exponents (α,β) on the (Z_iZ_s)- and mass-dependent factors as initial estimates (e.g. $\alpha\approx 0.4$, $\beta\approx 0.2$) and refine them with data [14, 16, 19, 20, 32].

A.2 Scaling of E_{th}

For a head-on elastic collision [1],

$$T_{\max} = \frac{4M_iM_s}{(M_i+M_s)^2}\,E, \tag{20}$$

and the threshold condition $T_{\max}(E_{\text{th}}) = U_s$ yields

$$E_{\text{th}} = \frac{(M_i+M_s)^2}{4M_iM_s}\,U_s = \frac{M_i+M_s}{4\,m_r}\,U_s. \tag{21}$$

Thus E_{th} scales with U_s and the mass combination $\frac{M_i+M_s}{m_r}$.

A.3 Scaling of λ

In the Eckstein model, λ controls how steeply the yield rises just above E_{th}. Near threshold, $Y(E) \propto s_n(E)\cdot(E/E_{th}-1)^{\mu}$. Since s_n contains all E-dependence via ε [Eq. (17)], and $\varepsilon = \frac{a_L E}{Z_i Z_s e^2}\frac{M_s}{M_i+M_s}$ so that the species-dependent factors (a_L, Z_i, Z_s, and $m_r = \frac{M_iM_s}{M_i+M_s}$) enter only through ε, we can write

$$\left.\frac{ds_n}{dE}\right|_{E\approx E_{th}} \propto \frac{ds_n}{d\varepsilon}\cdot\frac{d\varepsilon}{dE} \propto \frac{m_r}{Z_iZ_s\,a_L}. \tag{22}$$

Physically, a larger slope in s_n means a sharper onset, so λ is inversely related to this slope in a first-order approximation:

$$\lambda \propto \frac{Z_iZ_s\,a_L}{m_r}. \tag{23}$$

We use Eq. (11) only as a weak, physics-informed prior, allowing data to refine λ.

A.4 Scaling of μ

The sharpness exponent μ determines how steeply the yield increases beyond threshold. Unlike Q and E_{th}, there is no clear theoretical scaling for μ from LSS or Sigmund theory.

$$\mu_t = \mu_r. \tag{24}$$

In our approach, μ is kept fixed during the initial scaling step and refined in the Bayesian fitting stage when target-specific data are available.

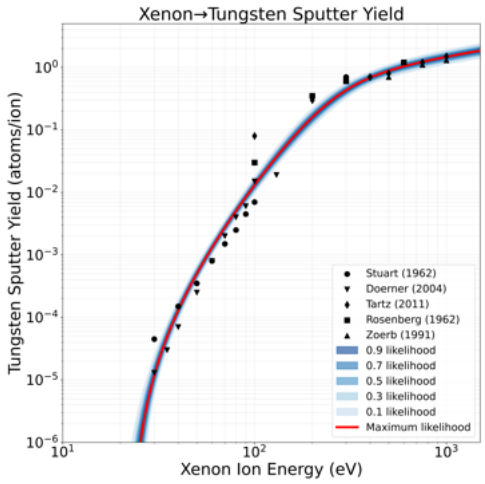
Xenon→Tungsten Sputter Yield
Tungsten Sputter Yield (atoms/ion)
Xenon Ion Energy (eV)
Stuart (1962)
Doerner (2004)
Tartz (2011)
Rosenberg (1962)
Zoerb (1991)
0.9 likelihood
0.7 likelihood
0.5 likelihood
0.3 likelihood
0.1 likelihood
Maximum likelihood

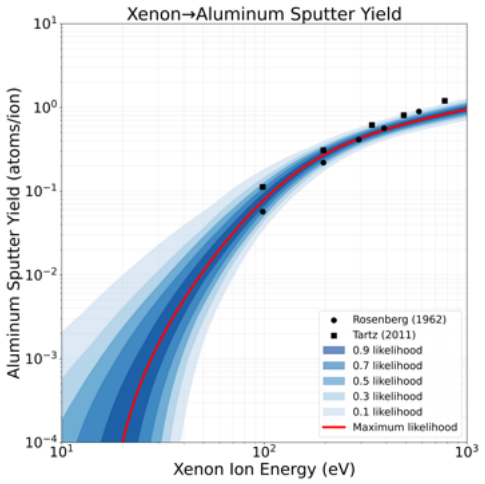
Xenon→Aluminum Sputter Yield
Aluminum Sputter Yield (atoms/ion)
Xenon Ion Energy (eV)
Rosenberg (1962)
Tartz (2011)
0.9 likelihood
0.7 likelihood
0.5 likelihood
0.3 likelihood
0.1 likelihood
Maximum likelihood

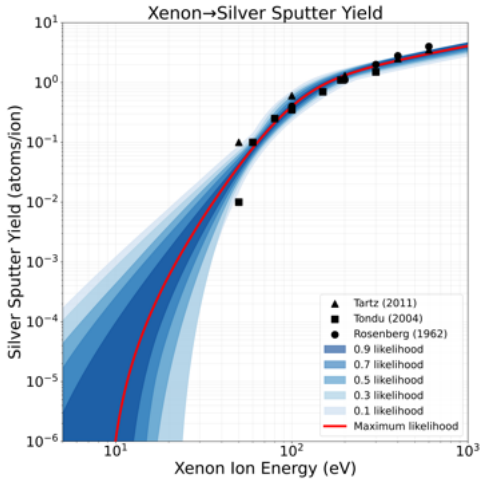
Xenon→Silver Sputter Yield
Silver Sputter Yield (atoms/ion)
Xenon Ion Energy (eV)
Tartz (2011)
Tondu (2004)
Rosenberg (1962)
0.9 likelihood
0.7 likelihood
0.5 likelihood
0.3 likelihood
0.1 likelihood
Maximum likelihood

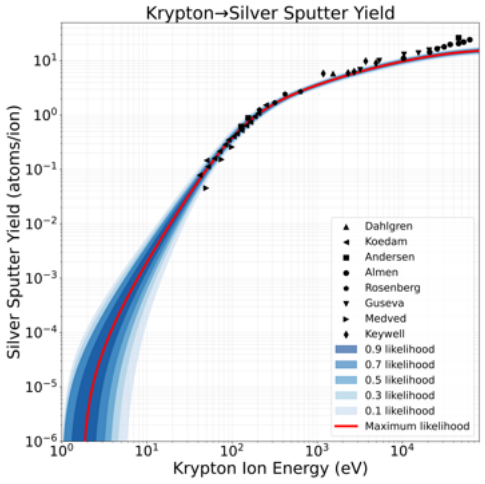
Krypton→Silver Sputter Yield
Silver Sputter Yield (atoms/ion)
Krypton Ion Energy (eV)
Dahlgren
Koedam
Andersen
Almen
Rosenberg
Guseva
Medved
Keywell
0.9 likelihood
0.7 likelihood
0.5 likelihood
0.3 likelihood
0.1 likelihood
Maximum likelihood

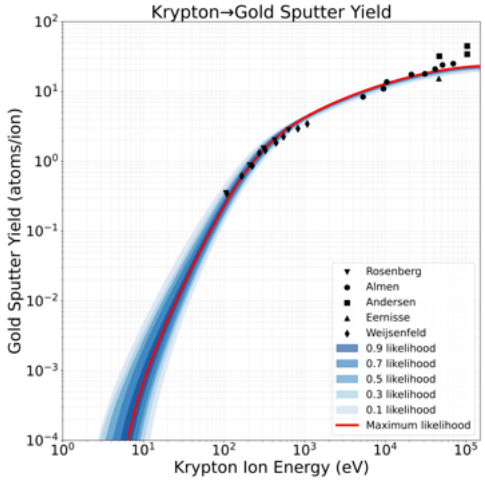
Krypton→Gold Sputter Yield
Gold Sputter Yield (atoms/ion)
Krypton Ion Energy (eV)
Rosenberg
Almen
Andersen
Eernisse
Weijsenfeld
0.9 likelihood
0.7 likelihood
0.5 likelihood
0.3 likelihood
0.1 likelihood
Maximum likelihood

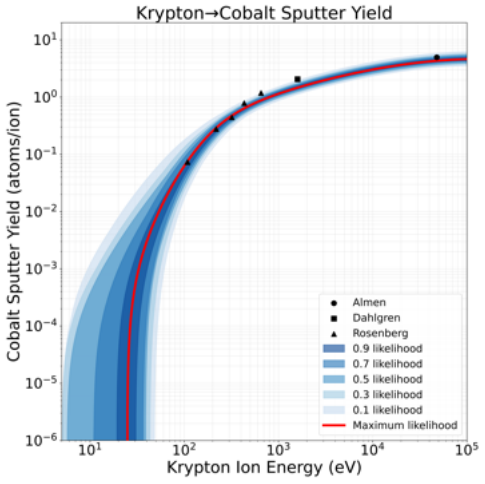
Krypton→Cobalt Sputter Yield
Cobalt Sputter Yield (atoms/ion)
Krypton Ion Energy (eV)
Almen
Dahlgren
Rosenberg
0.9 likelihood
0.7 likelihood
0.5 likelihood
0.3 likelihood
0.1 likelihood
Maximum likelihood

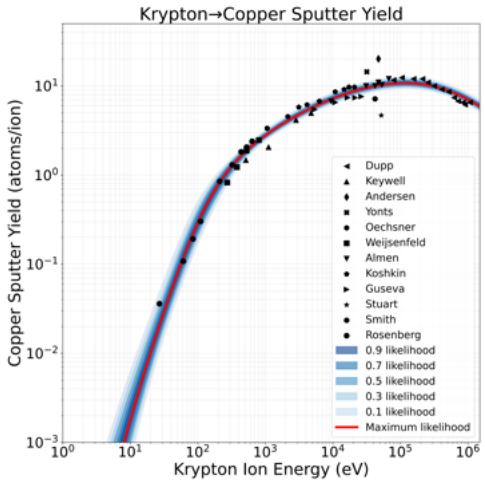
Krypton→Copper Sputter Yield
Copper Sputter Yield (atoms/ion)
Krypton Ion Energy (eV)
Dupp
Keywell
Andersen
Yonts
Oechsner
Weijsenfeld
Almen
Koshkin
Guseva
Stuart
Smith
Rosenberg
0.9 likelihood
0.7 likelihood
0.5 likelihood
0.3 likelihood
0.1 likelihood
Maximum likelihood

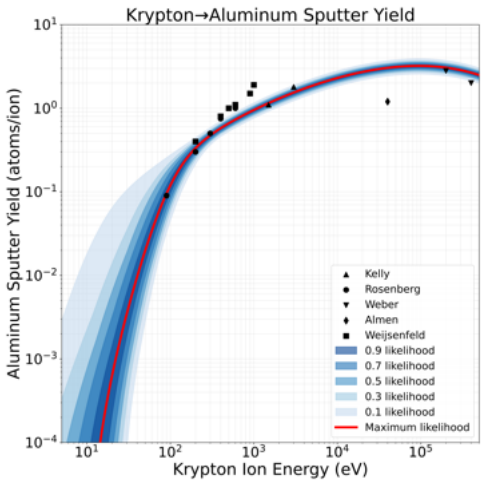
Krypton→Aluminum Sputter Yield
Aluminum Sputter Yield (atoms/ion)
Krypton Ion Energy (eV)
Kelly
Rosenberg
Weber
Almen
Weijsenfeld
0.9 likelihood
0.7 likelihood
0.5 likelihood
0.3 likelihood
0.1 likelihood
Maximum likelihood

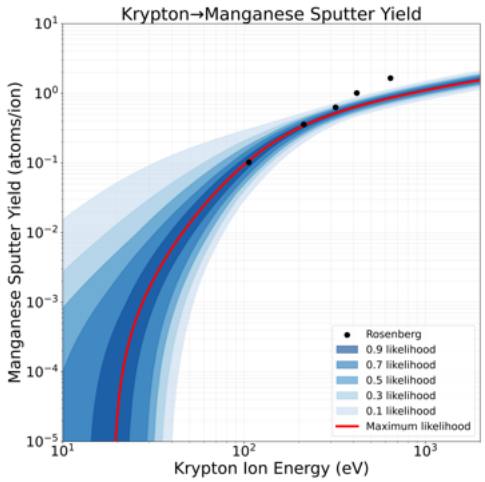
Krypton→Manganese Sputter Yield
Manganese Sputter Yield (atoms/ion)
Krypton Ion Energy (eV)
Rosenberg
0.9 likelihood
0.7 likelihood
0.5 likelihood
0.3 likelihood
0.1 likelihood
Maximum likelihood

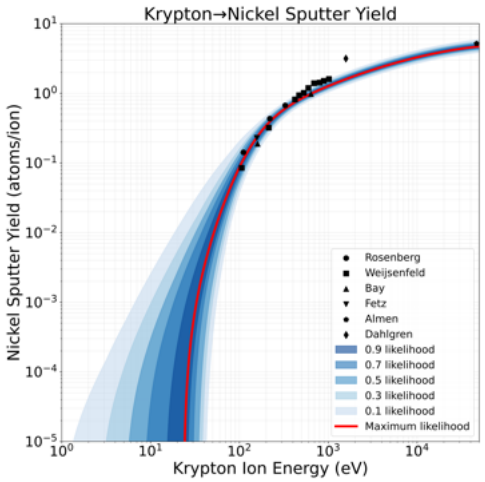
Krypton→Nickel Sputter Yield
Nickel Sputter Yield (atoms/ion)
Krypton Ion Energy (eV)
Rosenberg
Weijsenfeld
Bay
Fetz
Almen
Dahlgren
0.9 likelihood
0.7 likelihood
0.5 likelihood
0.3 likelihood
0.1 likelihood
Maximum likelihood

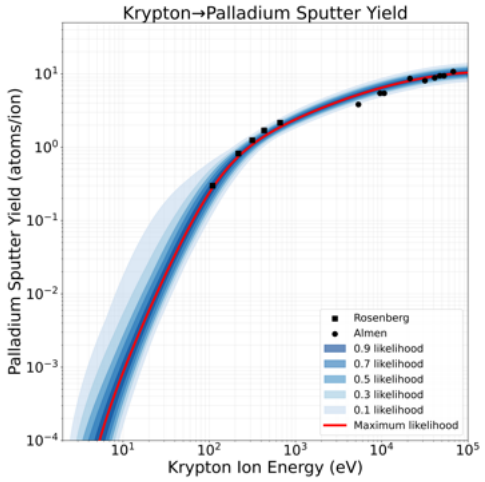
Krypton→Palladium Sputter Yield
Palladium Sputter Yield (atoms/ion)
Krypton Ion Energy (eV)
Rosenberg
Almen
0.9 likelihood
0.7 likelihood
0.5 likelihood
0.3 likelihood
0.1 likelihood
Maximum likelihood

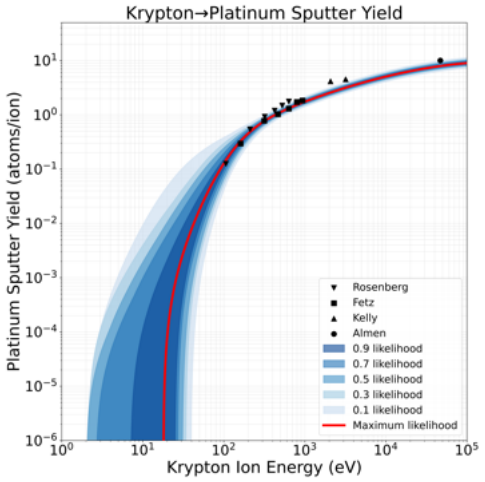
Krypton→Platinum Sputter Yield
Platinum Sputter Yield (atoms/ion)
Krypton Ion Energy (eV)
Rosenberg
Fetz
Kelly
Almen
0.9 likelihood
0.7 likelihood
0.5 likelihood
0.3 likelihood
0.1 likelihood
Maximum likelihood

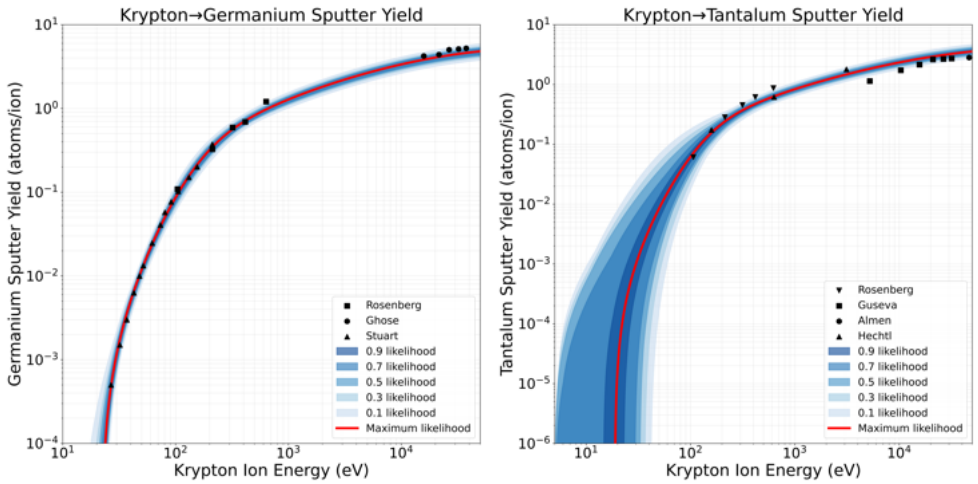
Krypton→Germanium Sputter Yield
Germanium Sputter Yield (atoms/ion)
Krypton Ion Energy (eV)
Rosenberg
Ghose
Stuart
0.9 likelihood
0.7 likelihood
0.5 likelihood
0.3 likelihood
0.1 likelihood
Maximum likelihood
Krypton→Tantalum Sputter Yield
Tantalum Sputter Yield (atoms/ion)
Krypton Ion Energy (eV)
Rosenberg
Guseva
Almen
Hechtl
0.9 likelihood
0.7 likelihood
0.5 likelihood
0.3 likelihood
0.1 likelihood
Maximum likelihood